# PROCEEDINGS OF SPIE

SPIEDigitalLibrary.org/conference-proceedings-of-spie

## Three-mirror freeform imagers

Jonathan C. Papa, Joseph M. Howard, Jannick P. Rolland

Jonathan C. Papa, Joseph M. Howard, Jannick P. Rolland, "Three-mirror freeform imagers," Proc. SPIE 10690, Optical Design and Engineering VII, 106901D (21 June 2018); doi: 10.1117/12.2314403



Event: SPIE Optical Systems Design, 2018, Frankfurt, Germany

### Three-mirror freeform imagers

Jonathan C. Papa\*a, Joseph M. Howardb, Jannick P. Rollanda
aThe Institute of Optics, University of Rochester, 275 Hutchison Road, Rochester, NY14627, USA;
bNASA Goddard Space Flight Center, Greenbelt, MD 20771, USA
\*jpapa@ur.rochester.edu

#### **ABSTRACT**

Driven by the development of freeform imaging systems, we have combined several concepts and techniques from the literature to analytically generate unobscured freeform starting point designs that are corrected through the third-order image degrading aberrations. The surfaces used in these starting point designs are described as a base off-axis conic that images stigmatically for the central field point, also known as a Cartesian reflector, with an aspheric departure "cap" (quartic with the aperture) added to the base off-axis conic to correct for the third-order image degrading aberrations. Once the aspheric caps are added to the surfaces, the system is then optimized using higher order freeform terms while leaving second-order terms frozen to preserve the focal length of the system during optimization. This technique is used to survey the three-mirror freeform imager solution space. Several systems that are the result of this technique are shown, with different numbers of internal images, internal pupil conjugates and folding geometries.

**Keywords:** Freeform, Telescopes, Mirrors, Aberrations, Conics

#### 1. INTRODUCTION

Using a combination of techniques from the literature, we analytically generate unobscured freeform starting point designs that are corrected through the third-order image degrading aberrations. These are systems with the object at infinity with a finite image conjugate. This method is used to automatically survey the 5-dimensional solution space of flat-field three-mirror freeform imagers. We evaluate the performance of the starting points using real raytraces and select the best performing systems for further optimization. In Section 2 we discuss the constraints that were applied to reduce the number of dimensions in the solution space. In Section 3 we show the best systems to come out of a survey run with a larger etendue.

The sag of the analytically designed freeform surfaces generated here can be decomposed into the base Cartesian reflector sag, and the aspheric cap (quartic with the aperture). Cartesian reflectors are off-axis conics that are used about the conic foci, such that for the central field point along the optical-axis-ray (OAR), or base ray, there is stigmatic imaging. A chain of Cartesian reflectors creates a system of confocal conics, where the conic focus coming out of one surface is coincident with the conic focus going into the next surface. Confocal conic systems do not have spherical aberration of any order, nor any other field-constant aberration of any order because there is always a node at the center of every aberration field. Confocal conic systems are not anamorphic [1].

In a rotationally-symmetric system, conics are often described by the parameters R and k, where R is the radius of curvature about the vertex and k is the conic constant. For Cartesian reflectors being used at a non-zero angle of incidence. It is convenient to describe the surface shape in terms of the distances to the stigmatic imaging points, the object distance and image distance, and the angle of incidence with respect to a local coordinate system where the sag and slope of that surface is zero at the origin of the local coordinate system. The analytically designed systems have surfaces that can be described by

$$Sag(x,y) = Sag_{Cartesian\ Reflector}(l_0, l_i, \theta, x, y) + A(x^2 + y^2)^2, \tag{1}$$

where Sag(x, y) is the total sag of the surface in the local coordinate system as a function of local coordinates x and y.  $Sag_{Cartesian\ Reflector}(l_o, l_i, \theta, x, y)$  is the sag of the Cartesian reflector as a function of object and image distances,  $l_o$  and  $l_i$ , angle of incidence of the OAR,  $\theta$ , and the local coordinates x and y. The aspheric cap coefficient, A specifies the magnitude of the surface term that is quartic with radial coordinate of the surface. Figure 1 shows raytraces for the three different Cartesian reflectors. Note that the aspheric cap is centered about the origin of the local coordinate system and not the axis of rotational symmetry for the conic; this breaks the rotational symmetry, making the surface a freeform surface [2].

Optical Design and Engineering VII, edited by Laurent Mazuray, Rolf Wartmann, Andrew P. Wood, Proc. of SPIE Vol. 10690, 106901D · © 2018 SPIE CCC code: 0277-786X/18/\$18 · doi: 10.1117/12.2314403

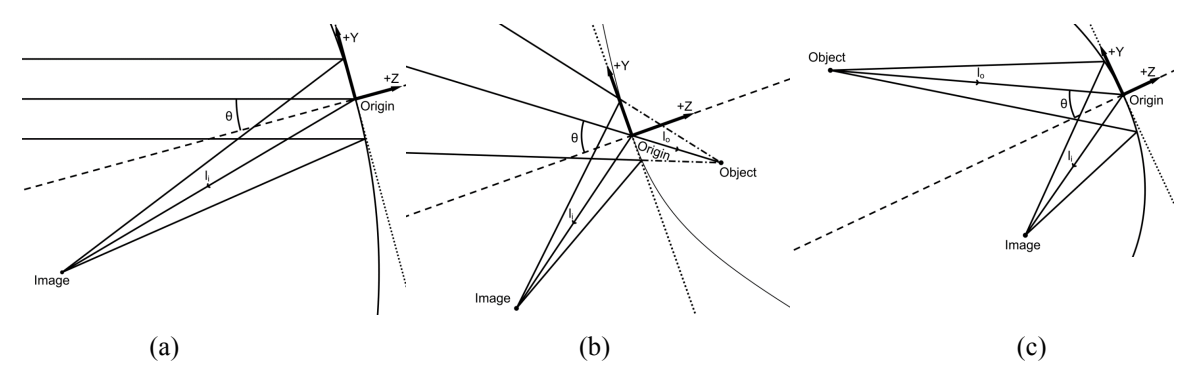


Figure 1. The local coordinate systems of the Cartesian reflectors, with the z axis normal to the surface. The conjugate distances for the object and image are labelled as  $l_o$  and  $l_i$ , respectively. The angle of incidence of the OAR is labelled as  $\theta$ . (a) parabolic Cartesian reflector, (b) hyperbolic Cartesian reflector, and (c) elliptical Cartesian reflector.

#### 2. CONSTRAINTS TO REDUCE THE DEGREES OF FREEDOM

The three-mirror systems we are generating analytically are described by 15 parameters. To reduce the number of dimensions of the solution space, we constrain some of the parameters to meet first-order specifications, as well as second and third-order image degrading aberration constraints. Figure 2(a) illustrates the 15 parameters, and Figure 2(b) illustrates which 10 parameters are constrained, and which five are free.

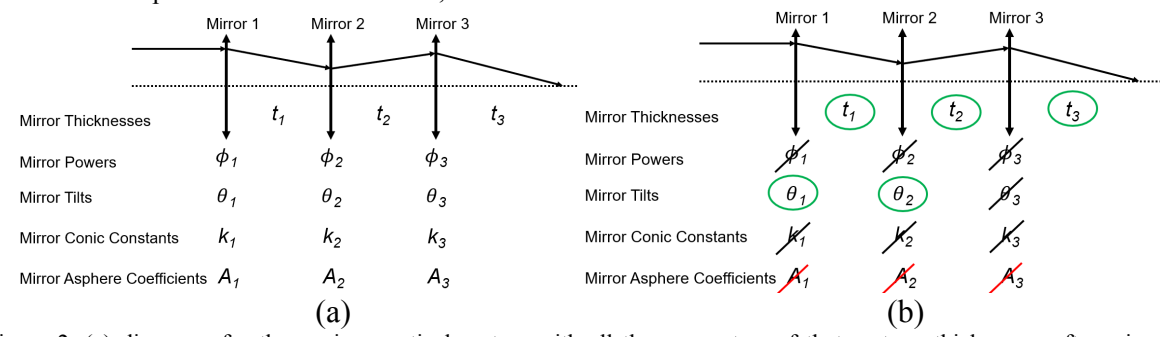


Figure 2. (a) diagram of a three-mirror optical system with all the parameters of that system: thicknesses after mirrors, mirror powers, mirror tilts, mirror conic constants, and mirror aspheric cap coefficients. There are 15 parameters. (b) the same diagram with constrained parameters crossed out, leaving five parameters that are needed to define the optical system.

In Figure 3, a block diagram shows how the parameters are solved for, and which constraints are applied. For first-order specifications, given the thicknesses after each mirror as inputs and the effective focal length and flat field applied as constraints, the power of all three mirrors are solved for. With the first-order parameters determined, they become the inputs that are needed to solve for the magnitude of the aspheric caps on all three mirrors, applying the constraints that third-order spherical aberration, field-linear coma, and field-quadratic astigmatism are zero. The first-order parameters as well as the tilts on the first two mirrors are used as inputs to solve for the tilt on the third mirror, applying the constraint that the second-order aberration field-linear astigmatism is zero.

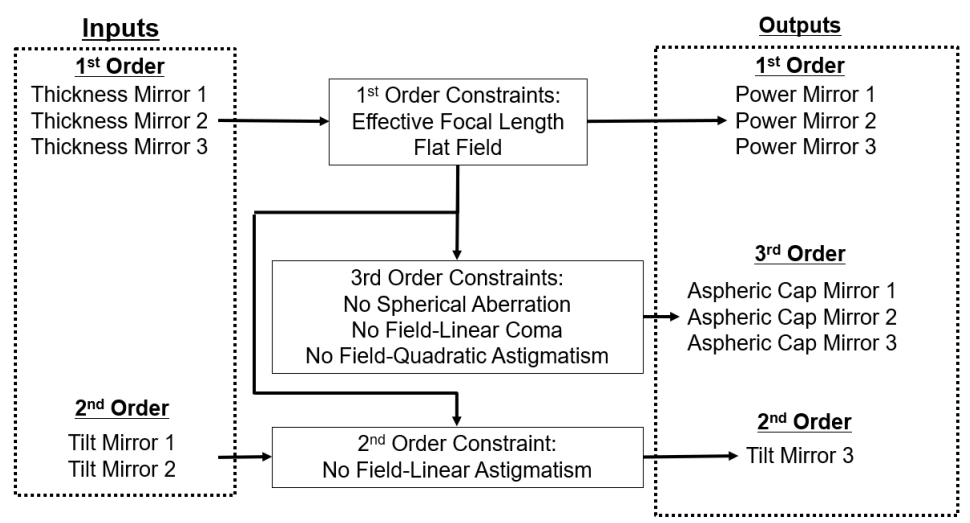


Figure 3. Block diagram demonstrating how constraints are applied to solve for certain system parameters.

#### 2.1 First-order constraints

We have chosen to use the thickness after each mirror and the tilts on the first two mirrors as the five free parameters. This allows the designer to directly manipulate the package size and folding geometry while holding the effective focal length constant. The third mirror power, denoted  $\phi_3$ , is constrained to hold the back focal length, the thickness from the last mirror to the image plane, at the value set by the designer:

$$\phi_3(\phi_1, t_1, t_2, t_3, efl) = \frac{-efl(1 + \phi_1 t_1) - t_2 + t_3}{t_2 t_3},$$
(2)

where  $\phi_1$  is the power on the first mirror,  $t_1$  is the thickness after the first mirror to the second mirror,  $t_2$  is the thickness after the second mirror to the third mirror,  $t_3$  is the thickness after the third mirror to the image plane, and efl is the effective focal length of the system. The second mirror power, denoted by  $\phi_2$ , along with the third mirror power, is constrained to hold the effective focal length of the system at the value set by the designer:

$$\phi_2(\phi_1, \phi_3, t_1, t_2, efl) = \frac{1 + efl(\phi_1 + \phi_3 + \phi_1 \phi_3 (t_1 - t_2))}{efl(1 + \phi_1 t_1)(\phi_3 t_2 - 1)}.$$
(3)

The powers of the second and third mirrors are functions of the power on the first mirror. To ensure that the solution is flat-field, the mirror powers must be balanced to eliminate Petzval field curvature. The first mirror power is constrained to be equal to the negative of the sum of the second and third mirror powers, and the first mirror power is solved for:

$$\phi_{1}(t_{1}, t_{2}, t_{3}, efl) = -\frac{2 efl + t_{2} - 2 t_{3} \pm \sqrt{\left(\frac{t_{2}}{efl t_{1}}\right) \left(efl t_{1} t_{2} + 4 efl t_{3} \left(efl - t_{1} + t_{2}\right) - 4 efl \left(2 t_{3}^{2} - t_{3}^{3}\right)\right)}}{2 \left(efl t_{1} - t_{2} t_{3}\right)}.$$

$$(4)$$

The constraint was a quadratic equation with two roots. The solution with the positive sign in front of the square root will be referred to as flat field solution 1, and the solution with the negative sign in front of the square root will be referred to as flat field solution 2.

#### 2.2 Second-order constraints

Nodal aberration theory predicts that it is possible to find tilted/decentered systems that exhibit aberrations of the "ordinary" kind, meaning that the two astigmatism nodes collapse to one node in the center of the field, which is also coincident with the coma node [3,4]. In the case of confocal conic systems, the only aberration that is not "ordinary" is field-asymmetric field-linear astigmatism; which can be eliminated by constraining the tilt on the last mirror [1]. From the literature there is a condition for zero field-linear astigmatism in a system of confocal conics [5], given each mirrors magnification and tilt angle, which is also the angle of incidence of the OAR that satisfies

$$\sum_{p=1}^{N-1} \left[ (1+m_p) \tan i_p \prod_{q=p+1}^{N} m_q \right] + (1+m_N) \tan i_N = 0, \tag{5}$$

where  $m_p$  is the magnification of the  $p^{th}$  mirror,  $i_p$  is the tilt of the  $p^{th}$  mirror,  $m_q$  is the magnification of the  $q^{th}$  mirror,  $m_N$  is the magnification of the last mirror, and  $i_N$  is the tilt of the last mirror. Using Equation 5, the tilt on the last mirror is constrained to keep field-linear astigmatism at zero. To determine the third mirror tilt, it is necessary to have the first-order specifications and first two mirror tilts set, as seen in Figure 3.

#### 2.3 Third-order constraints

Once field-linear astigmatism is eliminated, the remaining image degrading aberrations are field-linear coma and field-quadratic astigmatism [1,6]. These aberrations can be eliminated by introducing and canceling spherical aberration at the surfaces in the right combination. This is accomplished by adding the aspheric caps, centered about where the OAR intersects the surface and not the axis of rotational symmetry of the conic. Solving for the magnitude of the aspheric caps is a system of linear equations [7]:

$$\begin{bmatrix} 1 & 1 & 1 \\ 4\left(\frac{\overline{y_1}}{y_1}\right) & 4\left(\frac{\overline{y_2}}{y_2}\right) & 4\left(\frac{\overline{y_3}}{y_3}\right) \\ 4\left(\frac{\overline{y_1}}{y_1}\right)^2 & 4\left(\frac{\overline{y_2}}{y_2}\right)^2 & 4\left(\frac{\overline{y_3}}{y_3}\right)^2 \end{bmatrix} \begin{bmatrix} \Delta W_{040_1} \\ \Delta W_{040_2} \\ \Delta W_{040_3} \end{bmatrix} = \begin{bmatrix} \Delta W_{040} \\ \Delta W_{131} \\ \Delta W_{222} \end{bmatrix}, \tag{6}$$

where  $\overline{y_1}$  is the height of the paraxial chief ray on surface 1,  $y_1$  is the height of the paraxial marginal ray on surface 1,  $\Delta W_{040_1}$  is the spherical aberration introduced by the aspheric cap on surface 1,  $\Delta W_{040}$  is the total change in spherical aberration for the system,  $\Delta W_{131}$  is the total change in field-linear coma for the system,  $\Delta W_{222}$  is the total change in field-quadratic astigmatism for the system,  $\Delta W_{311}$  is the total change in field-cubic distortion for the system. The vector on the right-hand side is replaced with the negative of the aberration coefficients in the first-order, layout made of Cartesian reflectors. This system is solved for the vector on the left-hand side to get the amount of spherical aberration needed at each surface, and thus the amount of aspheric deviation needed at each surface. The paraxial ray data is obtained from a thin lens equivalent system with the same powers and mirror separations as the system of Cartesian reflectors.

The aspheric caps are necessary because a system of only Cartesian reflectors cannot have zero field-linear coma and field-quadratic astigmatism, unless the system is afocal or has a magnification with an absolute value of 1 [8].

#### 2.4 Sign convention of tilts

To classify the folding geometries of the systems in the survey, a sign convention is adopted where a counter-clockwise tilt from normal incidence of the OAR is referred to as "P" for positive, and a clockwise tilt from normal incidence of the OAR is referred to as "N" for negative. A three-letter sequence is used to denote the tilts of the first, second, and third mirrors respectively. Figure 4 shows a "PNP" system.

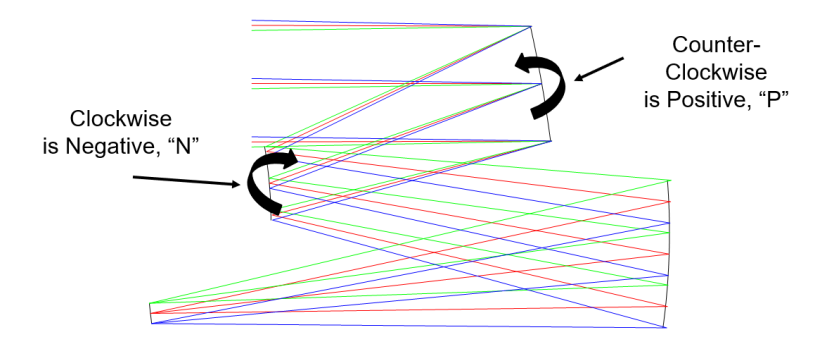


Figure 4. Three-mirror system to illustrate the sign convention used to describe the direction of tilt in this work.

#### 2.5 Checking for obstruction with polygons

To save computation time in the automated survey, systems that are obstructed were not analyzed with real raytraces, which are the most computationally expensive part of the process. To determine which systems are obstructed, a set of either one, two, or three polygons is used to enclose the set of rays between surfaces, which are drawn with thick black lines in Figure 5: what is needed is one polygon if there is no internal pupil nor an internal image, two polygons if there

is one internal pupil or one internal image, and three polygons if there are both an internal pupil and an internal image. For each surface, which includes all the mirrors plus the image plane, it is determined if the surface is inside of any the polygons, excluding polygons characterizing the set of rays going into or out of the surface under consideration. In Figure 5, the image plane is obstructing the system.

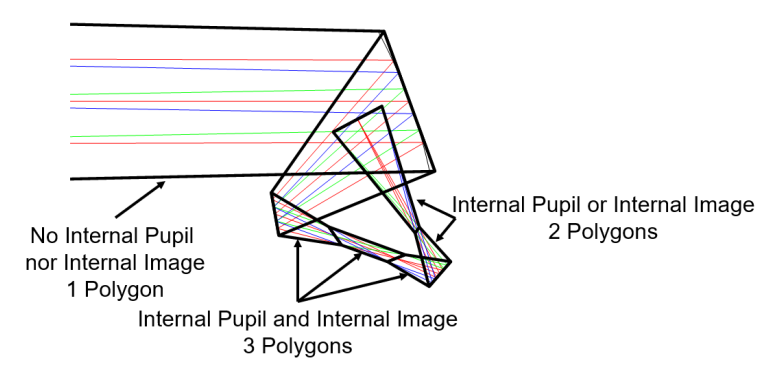


Figure 5. Three-mirror system to illustrate how it is determined that a system is obstructed.

#### 3. SURVEY RUNS

#### 3.1 Possible cases and sampling of solution space parameters

One can enter either a positive or negative focal length into Equations 2, 3, and 4. Additionally, one can choose either flat field solution 1 or flat field solution 2, resulting in four different first-order layouts. For this survey we focused on systems with the aperture stop at the first mirror, but including configurations with the aperture stop on the second and third mirror, there are then 12 different possibilities. The surveys use five nested for loops to cycle through different values of the five input parameters, illustrated in Figure 6.

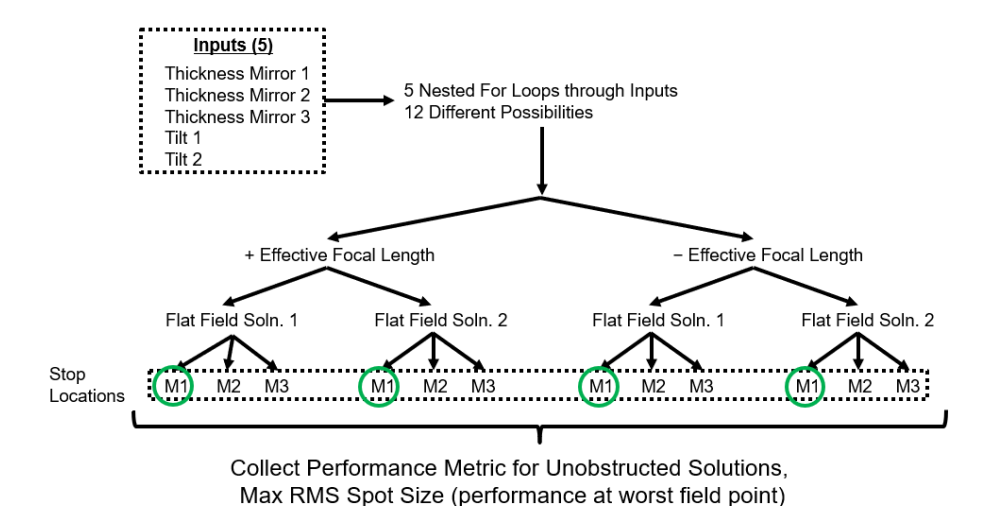


Figure 6. Tree of the possible first-order configurations that will require separate survey runs.

We chose a system effective focal length of 100 mm. Table 1 lists the sampling of the five input parameters. Tilt 1 was only sampled from 0 to 45 degrees instead of -45 to 45 degrees because having positive and negative values for the first mirror is redundant. For this survey we consider tilt angles larger than 45 degrees to be too large. When the tilt on the third mirror, which is solved for, exceeded 45 degrees the system was filtered out. The sampling from Table 1 results in 65,170 different input parameter combinations, which is repeated for four possible first-order configurations, meaning

260,680 systems were considered in each survey. We ran two surveys, one with a smaller etendue and one with a larger etendue.

Table 1. The boundary and sampling of the parameters of the solution space.

Parameter	Minimum	Maximum	Step Size	Number of Steps
Thickness 1 (mm)	-150	-30	20	7
Thickness 2 (mm)	30	150	20	7
Thickness 3 (mm)	-150	-30	20	7
Tilt 1 (deg.)	0	45	5	10
Tilt 2 (deg.)	-45	45	5	19

#### 3.2 Expected folding geometries

We expected the surveys to contain a variety of unobscured folding geometries, as illustrated in Figure 7. Figure 7 classifies the systems not only based on the signs of the tilts of the mirrors, but also where the mirrors and image plane are located relative to each other qualitatively. The columns of Figure 7 represent different locations of the image plane. The rows of Figure 7 represent different locations of the third mirror.

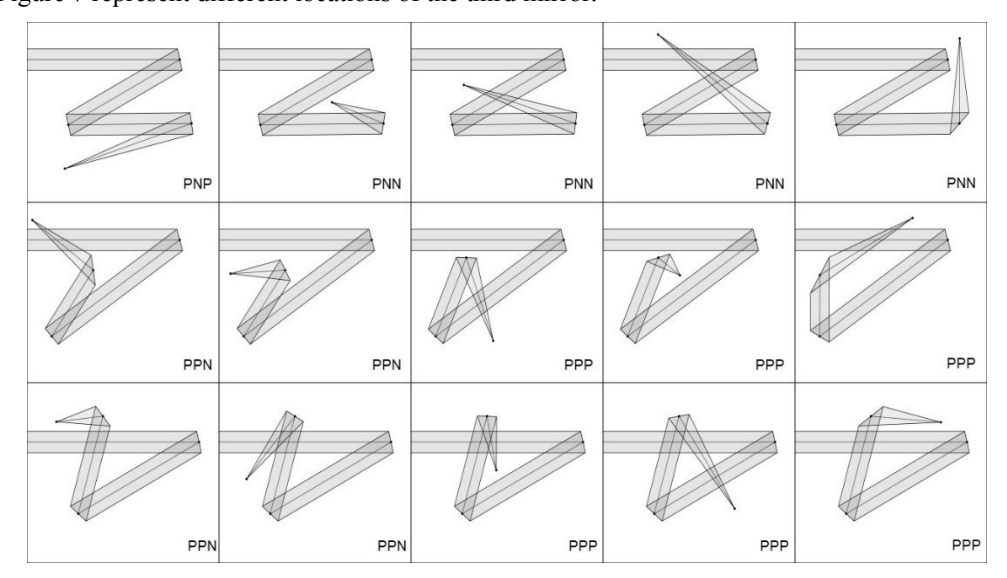


Figure 7. This figure qualitatively illustrates all the different folding geometries that are expected to be found within the survey. Next to each geometry are the signs of the tilts of the mirrors denoted with the notation described in Section 2.4, illustrated in Figure 4.

#### 3.3 Smaller etendue survey run

The systems in the smaller etendue survey had an effective focal length of 100 mm, a full field of view of 2 degrees by 2 degrees, and an aperture of F/5. Looking through the unobscured systems that were generated, all the qualitative folding geometries in Figure 7 were found except for the one in the first column, middle row. This is because we filtered out solutions with mirror tilt angles greater than 45 degrees. By ignoring this filter, a system matching that geometry was found manually by adjusting the systems free parameters. An example of each folding geometry from Figure 7 is found within the smaller etendue survey and displayed in Figure 8.

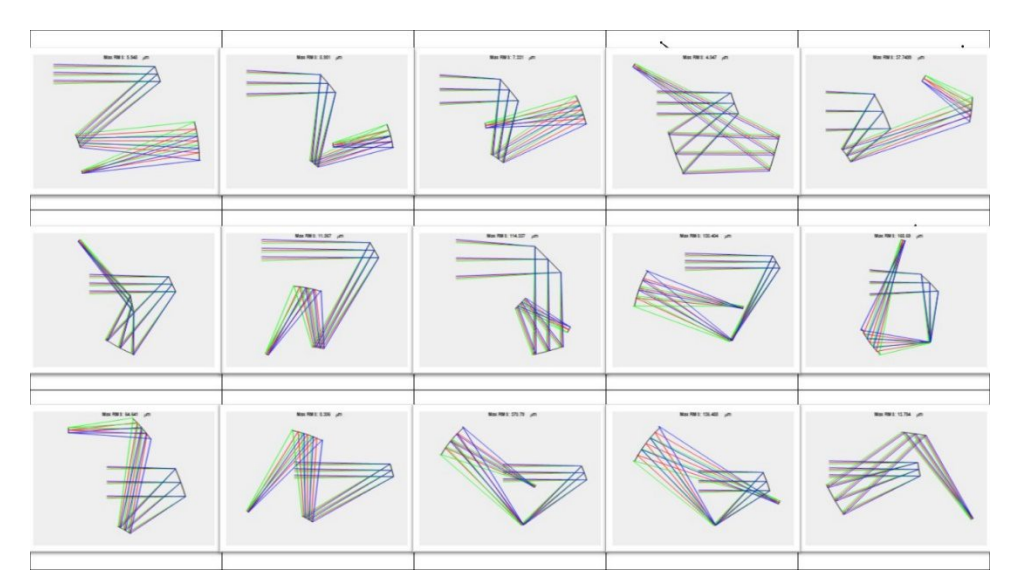


Figure 8. Examples of different folding geometries found within the survey, overlaid on top of the same table as Figure 7 to demonstrate that the survey contains almost all the folding geometries. The system in the first column, middle row was filtered out of the survey because the tilt angle on its third mirror exceeded 45 degrees.

The solutions with the smallest max RMS spot size from each of the four unique first-order layout branches, highlighted with green circles in Figure 6, were selected and optimized further varying the planar symmetric 3<sup>rd</sup> through 6<sup>th</sup> order XY polynomial freeform terms [9]. A histogram of the performance for the solutions in each branch and an optical layout of the best solution from each branch are shown in Figures 9 through 12. The performance of the best solution from each branch without aspheric caps, with aspheric caps, and optimized freeform terms is shown in Tables 2 through 5. The optical layouts in this manuscript were generated using paraxial approximations (rays are drawn to flat planes), but the performance was evaluated using real raytrace data.

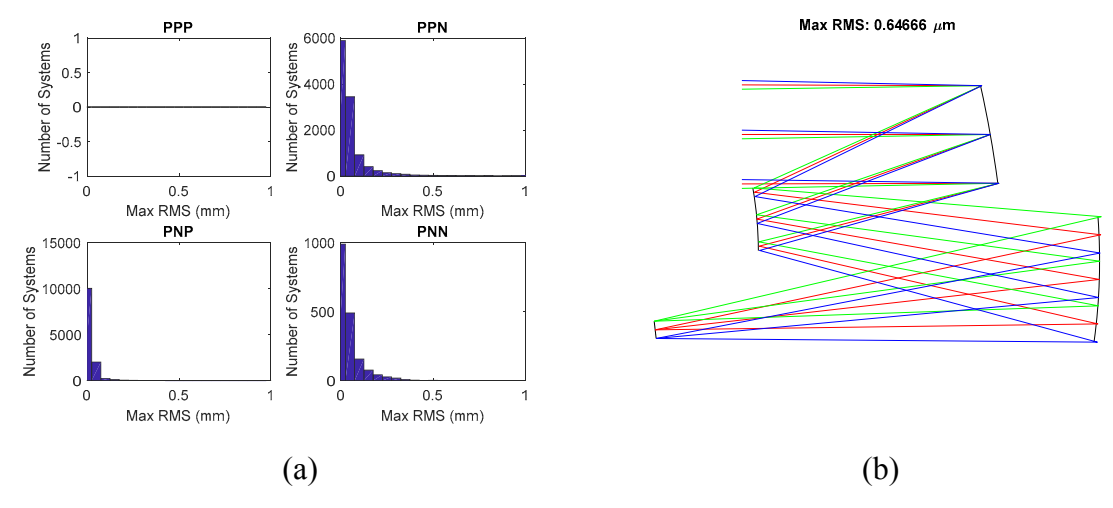


Figure 9. (a) Four performance histograms representing the four distinct tilt angle sign combinations for the survey run with an effective focal length of -100 mm, flat field solution 1, F/5, FFOV 2 degrees by 2 degrees. The systems are binned according to the worst field point RMS spot size. (b) An optical layout of the best performing, analytically designed system from this survey run, along with its max RMS spot size of 0.65 microns.

Table 2. The maximum, minimum, and average RMS spot size over the field for the system in Figure 9(b); without aspheric caps, with aspheric caps, and with optimization of planar symmetric XY polynomials terms  $3^{rd}$  through  $6^{th}$  order. Demonstrating the improvement of performance using analytically solved aspheric caps, and further improvements using higher order freeform terms.

	No Aspheric Caps	Aspheric Caps	3 <sup>rd</sup> through 6 <sup>th</sup> Order Optimized
Max RMS (μm)	13.76	0.65	0.08
Min RMS (μm)	0.00	0.23	0.03
Average RMS (µm)	7.68	0.40	0.05

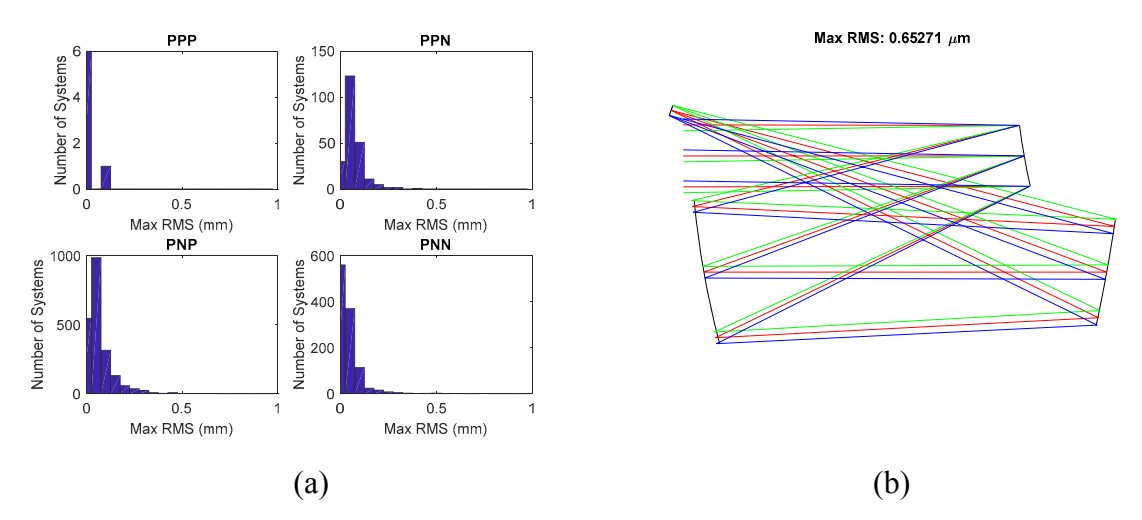


Figure 10. (a) Four performance histograms representing the four distinct tilt angle sign combinations for the survey run with an effective focal length of -100 mm, flat field solution 2, F/5, FFOV 2 degrees by 2 degrees. The systems are binned according to the worst field point RMS spot size. (b) An optical layout of the best performing, analytically designed system from this survey run, along with its max RMS spot size of 0.65 microns.

Table 3. The maximum, minimum, and average RMS spot size over the field for the system in Figure 10(b); without aspheric caps, with aspheric caps, and with optimization of planar symmetric XY polynomials terms 3<sup>rd</sup> through 6<sup>th</sup> order. Demonstrating the improvement of performance using analytically solved aspheric caps, and further improvements using higher order freeform terms.

	No Aspheric Caps	Aspheric Caps	3 <sup>rd</sup> through 6 <sup>th</sup> Order Optimized
Max RMS (μm)	10.30	0.65	0.06
Min RMS (μm)	0.00	0.16	0.02
Average RMS (µm)	6.18	0.35	0.04

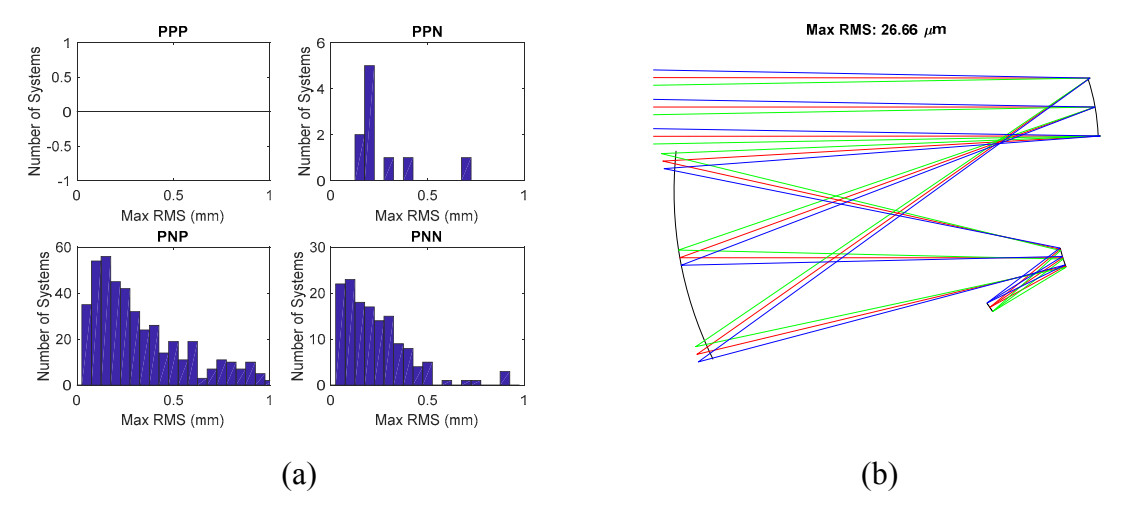


Figure 11. (a) Four performance histograms representing the four distinct tilt angle sign combinations for the survey run with an effective focal length of +100 mm, flat field solution 1, F/5, FFOV 2 degrees by 2 degrees. The systems are binned according to the worst field point RMS spot size. (b) An optical layout of the best performing, analytically designed system from this survey run, along with its max RMS spot size of 26.66 microns.

Table 4. The maximum, minimum, and average RMS spot size over the field for the system in Figure 11(b); without aspheric caps, with aspheric caps, and with optimization of planar symmetric XY polynomials terms 3<sup>rd</sup> through 6<sup>th</sup> order. Demonstrating the improvement of performance using analytically solved aspheric caps, and further improvements using higher order freeform terms.

	No Aspheric Caps	Aspheric Caps	3 <sup>rd</sup> through 6 <sup>th</sup> Order Optimized
Max RMS (μm)	26.62	26.66	1.36
Min RMS (μm)	0.00	17.03	0.21
Average RMS (µm)	11.49	21.07	0.63

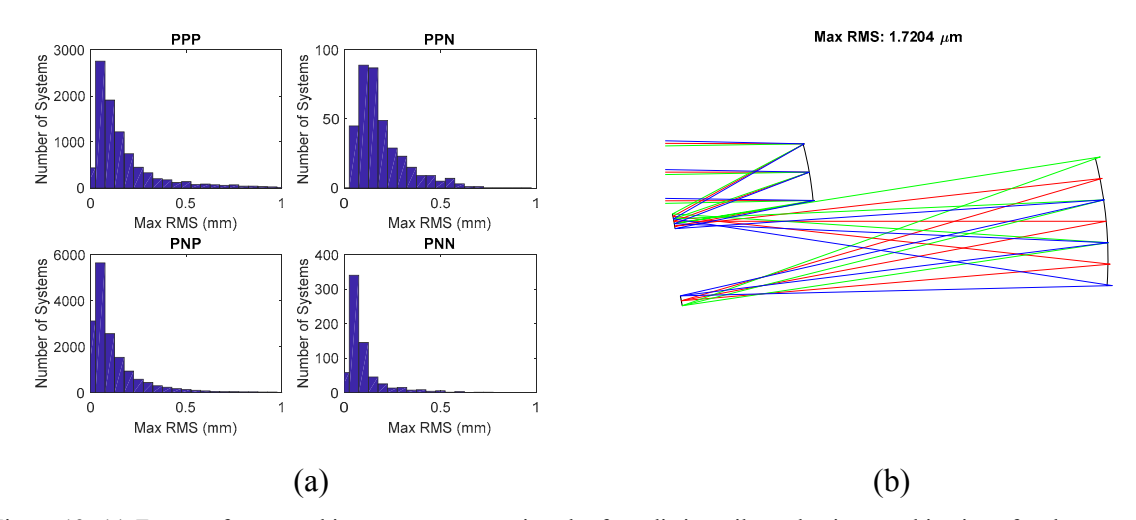


Figure 12. (a) Four performance histograms representing the four distinct tilt angle sign combinations for the survey run with an effective focal length of +100 mm, flat field solution 2, F/5, FFOV 2 degrees by 2 degrees. The systems are binned according to the worst field point RMS spot size. (b) An optical layout of the best performing, analytically designed system from this survey run, along with its max RMS spot size of 1.72 microns.

Table 5. The maximum, minimum, and average RMS spot size over the field for the system in Figure 12(b); without aspheric caps, with aspheric caps, and with optimization of planar symmetric XY polynomials terms 3<sup>rd</sup> through 6<sup>th</sup> order. Demonstrating the improvement of performance using analytically solved aspheric caps, and further improvements using higher order freeform terms.

	No Aspheric Caps	Aspheric Caps	3 <sup>rd</sup> through 6 <sup>th</sup> Order Optimized
Max RMS (μm)	33.31	1.72	0.08
Min RMS (μm)	0.00	0.13	0.01
Average RMS (μm)	15.10	0.99	0.04

#### 3.4 Larger etendue survey run

The systems in the larger etendue survey had an effective focal length of 100 mm, a full field of view of 4 degrees by 4 degrees, and an aperture of F/3. The solutions with the smallest max RMS spot size from each of the four unique first-order layout branches, highlighted with green circles in Figure 6, were selected and optimized further varying the planar symmetric 3<sup>rd</sup> through 6<sup>th</sup> order XY polynomial terms. A histogram of the performance for the solutions in each branch and an optical layout of the best solution from each branch are shown in Figures 13 through 16. The performance of the best solution from each branch without aspheric caps, with aspheric caps, and optimized freeform terms is shown in Tables 6 through 9.

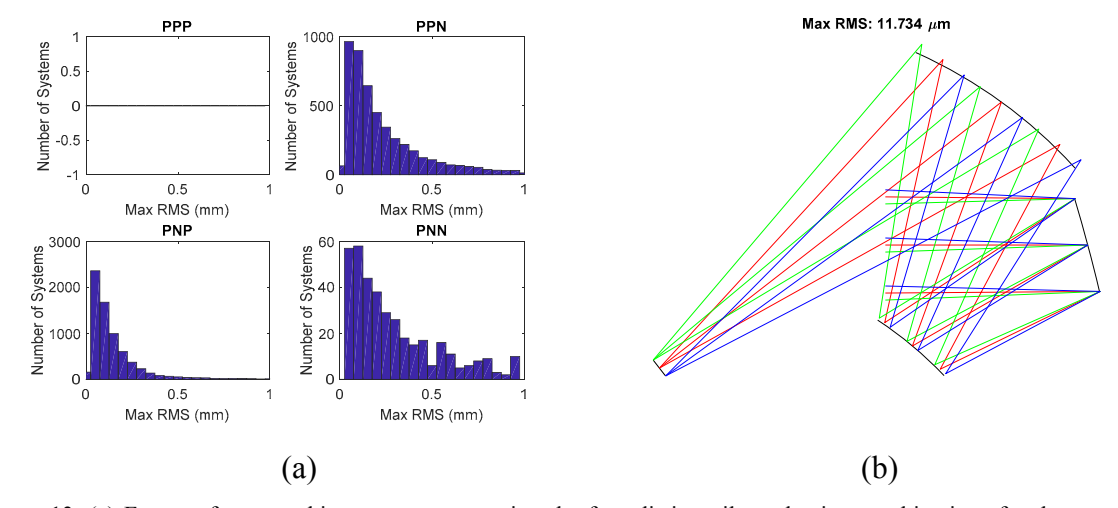


Figure 13. (a) Four performance histograms representing the four distinct tilt angle sign combinations for the survey run with an effective focal length of -100 mm, flat field solution 1, F/3, FFOV 4 degrees by 4 degrees. The systems are binned according to the worst field point RMS spot size. (b) An optical layout of the best performing, analytically designed system from this survey run, along with its max RMS spot size of 11.73 microns.

Table 6. The maximum, minimum, and average RMS spot size over the field for the system in Figure 13(b); without aspheric caps, with aspheric caps, and with optimization of planar symmetric XY polynomials terms 3<sup>rd</sup> through 6<sup>th</sup> order. Demonstrating the improvement of performance using analytically solved aspheric caps, and further improvements using higher order freeform terms.

	No Aspheric Caps	Aspheric Caps	3 <sup>rd</sup> through 6 <sup>th</sup> Order Optimized
Max RMS (μm)	80.01	11.73	3.06
Min RMS (μm)	0.00	4.79	1.00
Average RMS (μm)	42.12	7.21	1.72

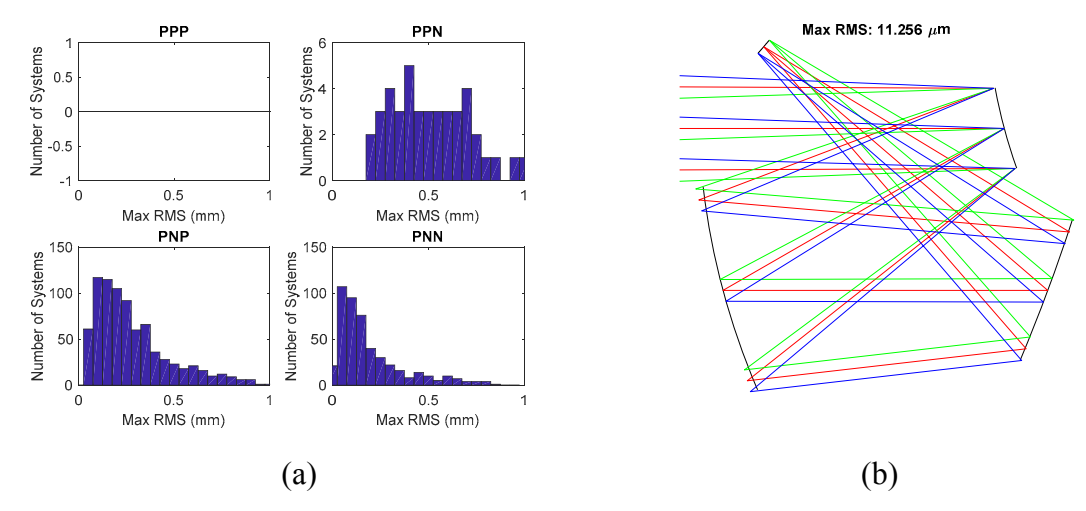


Figure 14. (a) Four performance histograms representing the four distinct tilt angle sign combinations for the survey run with an effective focal length of -100 mm, flat field solution 2, F/3, FFOV 4 degrees by 4 degrees. The systems are binned according to the worst field point RMS spot size. (b) An optical layout of the best performing, analytically designed system from this survey run, along with its max RMS spot size of 11.25 microns.

Table 7. The maximum, minimum, and average RMS spot size over the field for the system in Figure 14(b); without aspheric caps, with aspheric caps, and with optimization of planar symmetric XY polynomials terms 3<sup>rd</sup> through 6<sup>th</sup> order. Demonstrating the improvement of performance using analytically solved aspheric caps, and further improvements using higher order freeform terms.

	No Aspheric Caps	Aspheric Caps	3 <sup>rd</sup> through 6 <sup>th</sup> Order Optimized
Max RMS (μm)	59.96	11.26	1.06
Min RMS (μm)	0.00	1.33	0.28
Average RMS (µm)	34.89	4.70	0.68

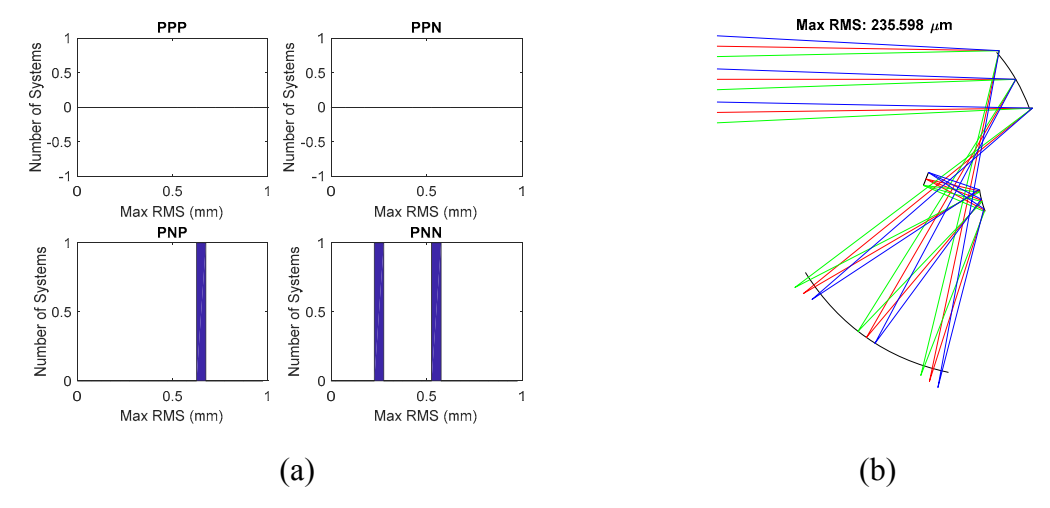
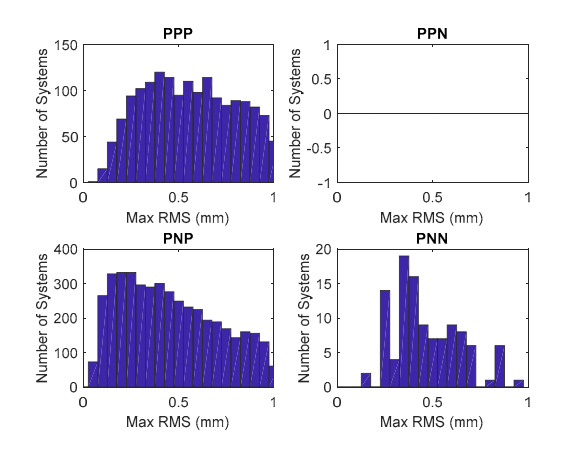


Figure 15. (a) Four performance histograms representing the four distinct tilt angle sign combinations for the survey run with an effective focal length of +100 mm, flat field solution 1, F/3, FFOV 4 degrees by 4 degrees. The systems are binned according to the worst field point RMS spot size. (b) An optical layout of the best performing, analytically designed system from this survey run, along with its max RMS spot size of 235.60 microns.

Table 8. The maximum, minimum, and average RMS spot size over the field for the system in Figure 15(b); without aspheric caps, with aspheric caps, and with optimization of planar symmetric XY polynomials terms 3<sup>rd</sup> through 6<sup>th</sup> order. Demonstrating the improvement of performance using analytically solved aspheric caps, and further improvements using higher order freeform terms. This system could not be optimized due to raytracing failures.

	No Aspheric Caps	Aspheric Caps	3 <sup>rd</sup> through 6 <sup>th</sup> Order Optimized
Max RMS (μm)	164.08	235.60	Ray Failures
Min RMS (μm)	0.00	73.09	Ray Failures
Average RMS (µm)	68.61	136.19	Ray Failures



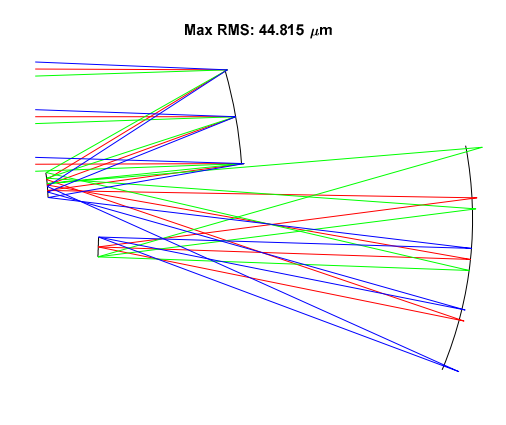


Figure 16. (a) Four performance histograms representing the four distinct tilt angle sign combinations for the survey run with an effective focal length of +100 mm, flat field solution 2, F/3, FFOV 4 degrees by 4 degrees. The systems are binned according to the worst field point RMS spot size. (b) An optical layout of the best performing, analytically designed system from this survey run, along with its max RMS spot size of 44.82 microns.

Table 9. The maximum, minimum, and average RMS spot size over the field for the system in Figure 16(b); without aspheric caps, with aspheric caps, and with optimization of planar symmetric XY polynomials terms 3<sup>rd</sup> through 6<sup>th</sup> order. Demonstrating the improvement of performance using analytically solved aspheric caps, and further improvements using higher order freeform terms.

	No Aspheric Caps	Aspheric Caps	3 <sup>rd</sup> through 6 <sup>th</sup> Order Optimized
Max RMS (μm)	305.28	44.81	2.54
Min RMS (μm)	0.00	0.99	0.77
Average RMS (μm)	129.58	19.05	1.44

#### 3.5 Discussion of survey results

Comparing the smaller and larger etendue surveys, the distribution of the histograms in Figures 9(a) through 16(a) show that the larger etendue analytically designed systems have a worse max RMS spot size, as is expected. Figure 17 shows the best analytically designed systems from each unique first-order branch, and also the performance after optimizing the 3<sup>rd</sup> through 6<sup>th</sup> order surface terms.

	Smaller Etendue			Smaller Etendue Larger Etendue			rger Etendue	
First Order Spec.	Layout	Max RMS (μm) Optimized	Rank	Layout	Max RMS (µm) Optimized	Rank		
EFL=-100 Flat Field 1		0.08	3		3.06	3		
EFL=-100 Flat Field 2		0.06	1		1.06	1		
EFL=+100 Flat Field 1		1.36	4		Ray Failure	4		
EFL=+100 Flat Field 2		0.08	2		2.56	2		

Figure 17. The best analytically designed systems from each unique first-order branch for the smaller and larger etendue survey. The performance after optimizing the 3<sup>rd</sup> through 6<sup>th</sup> order surface terms is shown as well as the rank of the performance relative to other systems in the survey after optimization.

It is interesting to note that the best analytical design form in the negative EFL, flat field solution 1 branch changed folding geometry going from a smaller to a larger etendue, while the folding geometry for the negative EFL, flat field solution 2 branch stayed the same going from a smaller to a larger etendue. The positive EFL, flat field solution 1 branch performed poorly, having a low number of unobscured systems compared to the other branches and max RMS spot sizes magnitudes of order worse than the other branches. This branch also did not improve with the introduction of aspheric caps, which may be due to higher-order aberrations from the relatively fast F/# on the first mirrors, and large tilts.

#### 4. SURVEY RUNS

The surveys contained a variety of design forms, which are similar to systems from the literature. In this section we comment on the similarities.

#### 4.1 Similarity to systems from literature [10]

In [Bauer, 2018] folding geometries where ranked by aberration correction potential for systems having a positive primary mirror, as seen in Figure 18.

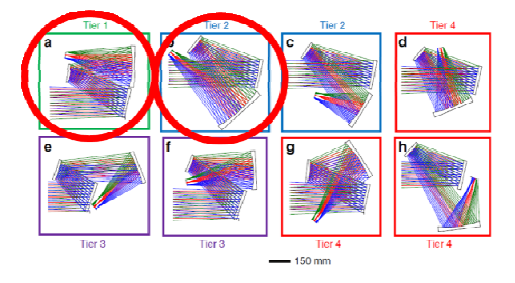


Figure 18. Figure adapted from [10] ranking the aberration correction potential for different folding geometries. Tier 1 systems have the best potential, while tier 4 has the worst. The systems circled in red were found within the current survey.

We found a similar system to the red circled tier 1 system in Figure 18 within the smaller etendue survey in the negative EFL, flat field solution 1 branch. It is similar in the sense that it has the same mirror power sequence (positive negative positive), as well as the same folding geometry. A system similar to the red circled tier 2 system in Figure 18 was found within the larger etendue survey in the negative EFL, flat field solution 1 branch. It is similar in the sense that it has the same mirror power sequence (positive negative positive), as well as the same folding geometry. It is interesting to note that these were the best analytically designed systems within the negative EFL, flat field solution 1 branch.

#### 4.2 Similarity to system from literature [11]

In [11] a freeform system with a negative primary mirror folded into a ball shape was designed. The optical layout of the system can be seen in Figure 19(a).

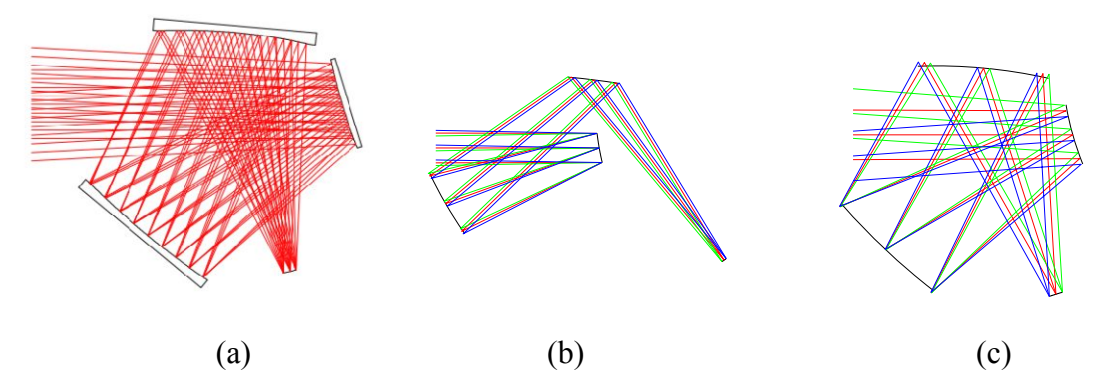


Figure 19. Optical layout (a) originally from [11]. (b) from similar system in the smaller etendue survey. (c) of system with parameters adjusted to match first-order specifications and to qualitatively match the form of the original system from [11].

Figure 19(b) shows a system found within the smaller etendue that has the same mirror power sequence (negative positive positive) and the same mirror tilt signs (PPP) as the original system from [11]. The parameters of the system from the survey were adjusted to have the same first-order specifications, and a qualitatively similar folding geometry. After optimizing the  $3^{rd}$  through  $6^{th}$  order surface terms the system in Figure 19(c) had the same performance as the original system (average RMS wavefront over the field of 0.008 waves at a wavelength of 10 microns).

#### 4.3 Similarity to system from literature [12]

In [12] a freeform system was designed with NURBS surfaces as seen in Figure 20(a).

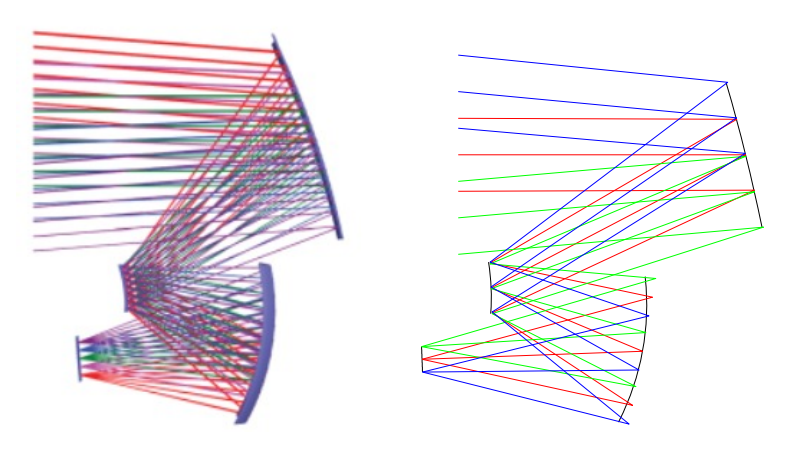


Figure 20. Optical layout (a) originally from [12]. (b) of similar system after parameter adjustment.

Figure 20(b) shows a system found within the smaller etendue survey that has been adjusted to have the same first-order specifications (i.e. F/2, 10 degrees by 9 degrees FFOV, 357 mm focal length) that has the same mirror power sequence (positive negative positive) and the same mirror tilt signs (PNP) as the original system from [12], and a qualitatively similar shape and the aperture stop on the second mirror. A circular pupil was assumed for the system in Figure 20(b). After optimizing the 2<sup>nd</sup> through 6<sup>th</sup> order surface terms the system in Figure 20(b) had an average RMS spot size of 11 microns, compared to the original system's performance of 14 microns average RMS spot size.

#### 5. CONCLUDING REMARKS

Using analytically generated starting points, we automatically surveyed the three-mirror freeform imager solution space, finding unobstructed solutions that are corrected through the third order image degrading aberrations. The survey contained the expected folding geometries except for those with high tilt angles because they were filtered out in the survey rules. In future work we plan to perform larger, higher resolution surveys of the three-mirror freeform solution space with the stop on the second and third surfaces. We also plan on applying the methods in this work to a four-mirror freeform imager solution space.

#### **ACKNOWLEDGEMENTS**

We acknowledge the NASA Space Technology Research Fellowship (NNX16AM90H) for supporting this research. We thank Synopsys Inc. for the student license of CODE V. This research synergizes with the NSF I/UCRC Center for freeform optics (IIP-1338877, IIP-1338898). We acknowledge Nicholas Takaki for helping to write the CODE V user defined surface DLL used in this work.

#### REFERENCES

- [1] Sasian, J. M., "How to Approach the Design of a Bilateral Symmetric Optical System," Opt. Eng. 33(6), 2045 (1994).
- [2] Papa, J. C., Howard, J. M., Rolland, J. P., "Starting point designs for freeform four-mirror systems," Proc. SPIE 10590, 105900Z (2017)
- [3] Thompson, K. P., "Aberrations fields in tilted and decentered optical systems," Ph.D. dissertation (University of Arizona, Tucson, Arizona, 1980)
- [4] Thompson, K. P., "Description of the third-order optical aberrations of near-circular pupil optical systems without symmetry," J. Opt. Soc. Am. A22, 1389-1401 (2005)
- [5] Chang, S., "Linear astigmatism of confocal off-axis reflective imaging systems with N-conic mirrors and its elimination," J. Opt. Soc. Am. A32, 852-859 (2015)
- [6] Rogers, J. R., "Vector Aberration Theory and The Design of Off-Axis Systems," Proc. SPIE 0554, 76-81 (1985).
- [7] Korsch, D., "Closed-form solutions for imaging systems, corrected for third-order aberrations," J. Opt. Soc. Am.63, 667-672 (1973)
- [8] Korsch, D. [Reflective Optics], Academic Press, Boston, 224-225 (1991).
- [9] Reshidko, D., Sasian, J., "Method for the design of nonaxially symmetric optical systems using free-form surfaces," Opt. Eng. 57(10) 101704 (2018)
- [10] Bauer, A., Schiesser, E. M., Rolland, J. P., "Starting geometry creation and design method for freeform optics," Nature Communications 9, 1756 (2018).
- [11] Fuerschbach, K., Rolland, J. P., Thompson, K. P., "A new family of optical systems employing φ-polynomial surfaces," Opt. Express 19(22), 21919-21928 (2011)
- [12] Chrisp, M. P., Primeau, B., Echter, M. A., "Imaging freeform optical systems designed with NURBS surfaces," Opt. Eng. 55(7) 071208 (2016)